Surface & Coatings Technology 512 (2025) 132367

Contents lists available at ScienceDirect

Surface & Coatings Technology

journal homepage: www.elsevier.com/locate/sct

Residual stresses induced by Inconel 718 cold gas repair spray of large cavities — On the influence of the sample geometry

Florian Lang [a,*], Johannes-Christian Schmitt [b], Thilo Pirling [c], Robert Vaßen [b], Jens Gibmeier [a]

[a] Institute for Applied Materials IAM-WK, Karlsruhe Institute of Technology, Kaiserstrasse 12, Karlsruhe, 76131, Germany
[b] Institute of Energy Materials and Devices IMD-2, Forschungszentrum Jülich GmbH, Wilhelm-Johnenstrasse, Jülich, 52425, Germany
[c] Institut Laue-Langevin, 71 Av. des Martyrs, Grenoble, 38000, France

ARTICLE INFO

Keywords:
Cold gas repair spray
Residual stress analysis
Neutron diffraction
Inconel 718

ABSTRACT

Following previous studies regarding the suitability of cold gas spray (CGS) for repairing large cavities in flat Inconel 718 components, circular specimen geometries were produced which contained tapered cavities with a depth of 4 mm. Two sets of process parameters, a hot and a cold parameter set, were used to fill the cavities with similar material by employing CGS. To evaluate the local residual stress state in the as-sprayed condition, non-destructive high-resolution neutron diffraction experiments were performed on the SALSA instrument at the Institut Laue-Langevin (ILL). 2D mappings of residual stress distributions were determined over the cross-sectional area in the centre of the specimens. Additionally, complementary laboratory residual stress analyses were carried out. The results of residual stress analyses indicate compressive residual stresses within the repaired zone, which are balanced by tensile residual stresses in the substrate adjacent to the repair site. Supplementary metallographic investigations show a good bonding between the repair filling and the substrate as well as strongly deformed particles within the repaired region. The latter indicates significant work hardening occurring during CGS. This is further supported by the increased widths of the diffraction lines recorded by neutron diffraction analyses and micro hardness distributions.

1. Introduction

Cold gas spray (CGS) is a well-established thermal spray process, combining solid phases in order to deposit materials that are either similar or dissimilar onto a substrate. Powder particles, typically with a diameter of $10\,\mu m \leq d_{particle} \leq 100\,\mu m$, are accelerated via a supersonic gas jet to velocities of up to $1500\,m\,s^{-1}$ and directed towards a substrate, where they form a dense coating [1–4]. The basic deposition mechanisms have been identified as a confined deformation due to the significant plastic deformation during impact, promoting mechanical interlocking and adiabatic shear instabilities, which leads to a removal of oxide scales and a metallurgical connection of the deposited particles even without melting [5–8]. To achieve the level of kinetic energy necessary to overcome the material specific critical velocity, the particles are mixed in a convergent–divergent nozzle with a pre-heated high-pressure gas. As the mixed gas–particle flow passes the de Laval nozzle, it is accelerated to supersonic speed, resulting in cooling of the gas. This is illustrated in the schematic in Fig. 1. It is essential to pre-heat the gas in order to increase the temperature of the particles and the sonic speed of the gas, thereby enabling the particles to be accelerated to higher velocities. For high-pressure CGS, the process gas is usually Nitrogen or Helium due to their thermodynamic properties, which are well-suited for the process [9,10].

In comparison to conventional thermal spray processes, CGS is regarded as a low-temperature process, as the deposition occurs in the solid state, rather than in the liquid or gaseous state, thereby minimising adverse effects resulting from phase transformation. Furthermore, it is a more environmentally friendly technique, as the power demand is relatively low and the use of toxic gases or chemicals is unnecessary [11–14]. CGS is a versatile process that can be used in a variety of applications. These include surface functionalisation, where it can be used to improve wear and corrosion resistance [15,16] or to develop antimicrobial surfaces [17]. Furthermore, it can be employed in the additive manufacturing of components [18–21]. Finally, it can be used in the repair of damaged components. Recently, there has been a notable increase in research activities within the field of aerospace component repair using CGS. For instance, the MOOG Aircraft Group observed that worn Inconel nose-wheel steering actuators repaired by means of CGS, exhibited superior corrosion resistance when compared

* Corresponding author.
E-mail address: Florian.Lang@kit.edu (F. Lang).

https://doi.org/10.1016/j.surfcoat.2025.132367
Received 14 October 2024; Received in revised form 7 March 2025; Accepted 2 June 2025
Available online 17 June 2025

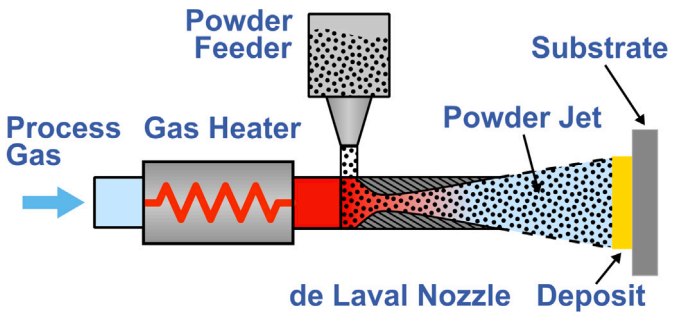

Fig. 1. Schematic diagram of the cold spray process.

to replacement parts [22]. In military aircraft, chafing around fastener holes in the aircraft skin leads to wear damage and the fit failing to meet tolerances. The use of CGS enabled the repair of skin panels using aluminium particles, thus avoiding the necessity for replacement and resulting in cost savings and the conservation of resources [23,24]. The repair of even larger defects on parts made from Inconel 718 presents an opportunity to expand the circular economy and thereby generate economic benefits, while simultaneously reducing the environmental impact.

The procedure for the repair of near-surface defects is illustrated in the schematic in Fig. 2: A near-surface damage, e.g. wear during operation, marks the initial state. In a first step, the defect is worked out, and the surface is prepared for the subsequent coating, i.e., cleaned and conditioned, similarly to other conventional repair techniques. The CGS is then used to deposit the repair material into the repair cavity. The last step is to machine the repair site to restore the final geometry in order to recover a restored component for recommissioning.

A comprehensive understanding of the interaction of CGS deposit with the component is essential for optimising performance and ensuring the durability of repaired components. Local residual stress (RS) distributions, which are crucial for assessing the structural integrity of such coating systems, represent a key area of investigation in CGS repair applications, particularly for large or deep defects. In the CGS repair of large cavities, there are three major effects contributing to the formation of RS in the coating system: a peening effect, due to the continuous particle impact on the surface, a temperature effect, due to thermal input and subsequent cooling of the surface, and a property mismatch resulting from differences in the physical properties of the materials involved. Depending on the material combination and specific CGS processing parameters, the resulting RS can be tensile or compressive. Boruah et al. [26], for example, found tensile RS in 4.5 mm high Ti–6Al–4V deposits on Ti–6Al–4V substrates. Vassen et al. [27] studied Inconel 718 coatings with different thicknesses deposited on Inconel 718 substrates by means of CGS. They found axisymmetric compressive RS depth profiles for all investigated coating thicknesses. Schmitt et al. [28] found that for the combination of thin full-surface layers of Inconel 718 particles deposited on Inconel 718 substrates, the resulting RS can effectively be adjusted by the appropriate choice of spraying parameters between tensile and compressive RS. While near-surface compressive RS can have a positive impact on the fatigue behaviour, for CGS applications high compressive RS can also cause delamination of the coating. The research of Singh et al. [29] shows, that the adhesion strength of Inconel 718 deposits on Inconel 718 substrates is influenced by the compressive RS state and the coating thickness. Fiebig et al. [30] concluded that the dependence of the adhesion strength on coating thickness for CGS Inconel 718 on Inconel 718 might effectively be affected by RS.

For the extension of CGS to the repair of substantial defects, particularly in Inconel 718 components intended for the use in turbine engines, it is crucial to examine the interaction between the repair site and the component in question. It is essential to ensure that the repair is fully and effectively bonded to the substrate. In order to evaluate the repair in terms of mechanical integrity in service, it is necessary to investigate the microstructure and analyse the RS. This is not only relevant for the filling, but also particularly for the interface and the component beyond. Given the intended application for the repair in aerospace components, which makes subsequent heat treatment challenging, it is important to ascertain whether the resulting repair properties can be controlled by suitable process parameters in case of filling confined cavities. Such an approach will ensure that the final repair is not susceptible to distortion and that it possesses adequate mechanical properties. Following our previous investigations into the suitability of CGS for the repair of defects with up to 4 mm depth on flat specimens made from Inconel 718 [25], this study extends the repair to large cavities on more practice relevant geometries, i.e. cylindrical specimens. The curvature causes different mechanical constraints that can influence the interaction of the CGS repair with the substrate. Elongated and tapered cavities with a depth of 4 mm were milled into the circumference of cylindrical Inconel 718 samples and subsequently filled by means of CGS using a powder feed stock with a chemical composition similar to Inconel 718 and two sets of processing parameters. The parameters mainly differ in the gas pressure and the gas temperature, in order to investigate the influence of different thermodynamic spraying conditions on the integrity of, and the resulting RS distribution in the repair of 4 mm deep cavities in Inconel 718 components. An assessment of the bonding of the filling to the substrate was conducted using microscopic analysis with a special focus on the interface region between repair site and substrate. The CGS repaired process zone was characterised in terms of hardness distribution and microstructure. Complementary RS analyses were conducted using incremental hole analysis, a destructive approach to analyse near-surface RS depth profiles on a laboratory scale, and non-destructive neutron diffraction experiments for in-depth RS analysis.

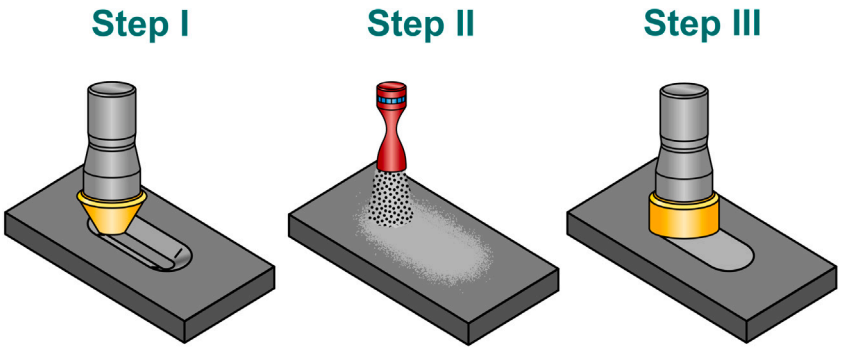

Fig. 2. Schematic sequence of component repair using the cold gas spray process (CGS): A surface damage is milled out and the surface is prepared (Step I). The filler material is deposited in the cavity by means of CGS (Step II). Afterwards, the component is re-machined to the final geometry (Step III) in order to produce a refurbished component for recommissioning.
Source: Modified from [25].

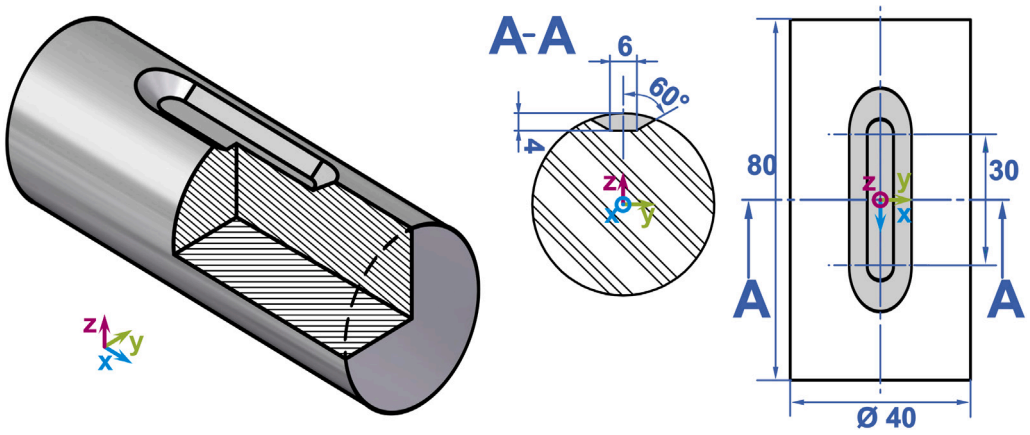

Fig. 3. Schematic showing the specimen geometry of the cylindrical samples and the corresponding sample coordinate system. All dimensions are given in mm.

Table 1
Selected CGS process parameters used to repair the specimens.

Sample designation	Gas pressure p_{gas}	Gas temperature T_{gas}
Parameter I	4 MPa	1223 K
Parameter II	4.5 MPa	1323 K

Although, neutron diffraction is limited to large-scale facilities, it is a particularly well suited method for the non-destructive analysis of RS stress distributions with a sufficiently high spatial resolution throughout the repair cavity and in the specimens. It is crucial to ascertain the distribution of RS in a repair cavity in its as-sprayed condition, i.e. without compromising the mechanical equilibrium, which can influence the final RS state. The combination of both methods provides a more comprehensive representation of the RS distribution, which extends from the surface of the repair site into the substrate beyond the interface. This is of significant importance for the assessment of the repair and the potential for distortion during a mechanical or thermal post-treatment, or during service operation.

2. Experimental

2.1. Sample preparation

Based on our findings in [25], this continuation of the research project focuses on a more practically relevant sample geometry. As most components exhibit some form of curvature, we were investigating a cylindrical specimen geometry. Two cylindrical rods made from Inconel 718 in an as-delivered solution annealed state (≈250 HV 10) were used as substrate material, with a length of $L_R = 80$ mm and a diameter of $\varnothing_R = 40$ mm. The cavities have a depth of $D_C = 4$ mm, a length of $L_C = 30$ mm and a width (in circumferential direction) of $W_C = 6$ mm at the bottom of the cavity, so that in the projection, the cavities have the same dimensions as in [25]. Using an angular milling cutter tool, the sidewalls of the cavities were tapered to an angle of $\alpha = 60°$ in order to improve the gas flow. Pre-trials showed an insufficient bonding of the repair filling to perpendicular sidewalls. As shown in [31], the incident angle plays a crucial role for the bonding and spray efficiency. Fig. 3 shows a schematic of the sample geometry with the repair cavity on the outer circumference and the sample coordinate system.

Two sets of spraying parameters were used to fill the cavities with AE10718 powder (Oerlikon-Metco, Troy, MI, USA) using CGS. The particles have a spherical morphology with a mean diameter of $d_{50} \approx 14$ µm and the same chemical composition as Inconel 718. In addition to the Inconel 718 particles, there are Al-rich Ni solid solution particles mixed in with the powder, in order to improve the deposition [32]. More details about the powder are given in Vassen et al. [27] and Singh et al. [33]. Using an Impact Gun 5/11 (Impact Innovations GmbH, Rattenkirchen, Germany), the 4 mm deep cavities were filled with 46 layers, arranged as a meander of 20 line profiles oriented along the length of the cavity. Fig. 4 shows pictures of the cylindrical specimens with the milled-out cavity (a) and the specimen processed with Parameter I in the as-sprayed condition (b). The specimens were processed at the Forschungszentrum Jülich. The spraying parameters mainly differ in the gas pressure and the gas temperature and are given in Table 1. The higher gas temperature for Parameter II is aimed at a lower compressive RS level in the CGS coating system and thereby reducing the risk of delamination and component distortion during a subsequent post-treatment or in-service operation. Prior to CGS coating, three preheating cycles were used to adapt the specimen surface to the gas temperature in order to increase the deformability of the substrate. This work focuses on investigating the specimens in the as-sprayed condition, after filling the repair site by means of CGS (cf. Step II in Fig. 2) and before the component is re-machined to the final geometry (cf. Step III in Fig. 2), as any alteration of the mechanical equilibrium can impact the resulting residual stress distribution.

2.2. Metallographic analyses

To assess the coating quality of the CGS repair filling as well as the bonding of the deposition to the surface of the repair cavities, metallographic analyses were performed on the mid-plane cross section of the repair cavity (cf. A-A reference in Fig. 3) sectioned by means of electrical discharge machining (EDM) wire cut. The samples were embedded in a two component universal embedding resin (VariKEM 200, Schmitz Metallographie GmbH, Herzogenrath, Germany) and then ground, polished and finally fine-polished using an oxide polishing suspension (OPS). Microstructure observations were performed using a Zeiss LEO 1530 scanning electron microscope (SEM) (Carl Zeiss Microscopy Deutschland GmbH, Oberkochen, Deutschland) in the backscattered electron (BSE) imaging mode with a magnification of 1000x. Micrographs were taken at several locations within the repair filling as well as along the interface.

2.3. Microhardness mapping

A mapping of the Vickers microhardness (HV 0.1) distribution was conducted for both parameters on the mid-plane cross section. Using a Q10 A+ hardness testing device (ATM Qness GmbH, Golling an der Salzach, Austria), a total of 2000 indentations were conducted according to the specifications outlined in DIN EN ISO 6507-1 [34]. The locations were arranged in a 22 mm × 5.5 mm grid adapted to the cross section of the cylindrical specimens with the distance between two indentations being $\Delta y = \Delta z = 250$ µm.

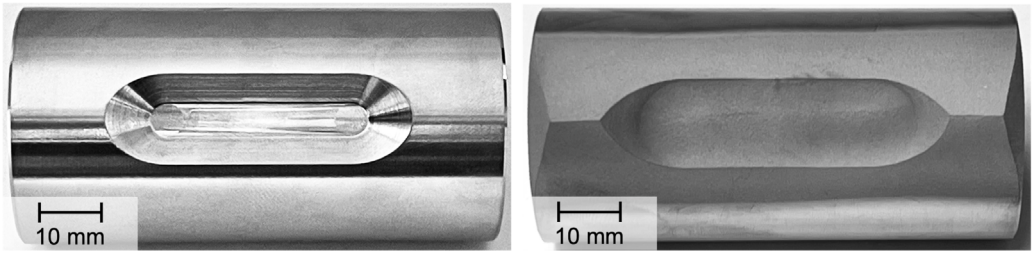

Fig. 4. Photographs showing the cylindrical specimens before CGS (a) and in the as-sprayed condition for Parameter I (b), showing overspray around the filled repair cavity.

2.4. Incremental hole drilling analysis

The incremental hole drilling method, a semi-destructive approach standardised by ASTM E837-20 [35], is widely used to analyse stress depth profiles. For this method, a blind hole is drilled gradually into the specimen in the area to be investigated. High-speed drilling methods are preferred, since conventional drilling induces undesirable residual stresses in the vicinity of the hole, which may corrupt the results. Material removal causes a redistribution of residual stresses around the blind hole and result in strain relaxation. This can be measured on the specimen surface using strain gauges placed at fixed angles (0°/45°/90°) around the blind hole. The residual stress state can be calculated from the measured strains. Depth profiles of the near-surface RS distribution were analysed in the centre of the repair cavity in the as-sprayed condition. A RS-200 Residual Stress Milling Guide (Micro-Measurements, Raleigh, NC, USA) in combination with TiN coated end mills with a nominal diameter $\varnothing_{mill} = 1.6\,\text{mm}$ were used for drilling. Strain relaxations at the surface were measured using strain gauge rosettes (Type B according to [35]) CEA-06-031-120 (Micro-Measurements, Raleigh, NC, USA). Prior to the application of the strain gauges, the surface at the measurement location had to be carefully ground to reduce the surface roughness after CGS. The RS calculation was performed using the differential approach outlined in [36], using the bulk values of the elastic constants $E = 204\,\text{GPa}$ and $\nu = 0.299$ for Inconel 718 according to Kröner [37], based on single crystal coefficients determined by Dye et al. [38].

2.5. Neutron diffraction

Neutron diffraction residual stress mappings were carried out at the SALSA instrument [39] located at the Institute Laue-Langevin, Grenoble, France. The analyses were carried out according to Hutchings [40] for both parameters in the as-sprayed condition in the three principal directions x, y and z, inferred from the specimen geometry (cf. Fig. 3). The dataset is available at Gibmeier et al. [41]. For measurements in y- and z-direction of the sample, the gauge volume was defined to $4\,\text{mm} \times 0.6\,\text{mm} \times 0.6\,\text{mm}$ using radial collimators (FWHM 0.6 mm), with the 4 mm in x-direction of the sample, to increase grain statistics while assuming a homogeneous distribution in this direction. For analysis in x-direction, the gauge volume was $2\,\text{mm} \times 2\,\text{mm} \times 0.6\,\text{mm}$. A wavelength of $\lambda \approx 1.63\,\text{Å}$ was set using the {422} reflection of a bent double focusing Si-crystal monochromator, resulting in $2\theta_0 \approx 97°$ for the γ-Ni {311} reflection of Inconel 718. A schematic of the instrument setup can be found in [25].

Using the described setup, triaxial RS mappings were performed at 26 positions, arranged in a grid on the mid-plane cross section of the cylindrical specimen (A-A ref. in Fig. 3). The grid spans an area of $-12.28\,\text{mm} \leq y \leq 0\,\text{mm}$ in y-direction and $14.5\,\text{mm} \leq z \leq 19\,\text{mm}$ in z-direction from the centre of the cavity into the surrounding substrate. Based on our findings for the RS distribution in large cavities filled by means of CGS in a previous work [25], we can assume symmetry of the RS distribution with respect to the y-direction of the sample. All data treatment was performed using the LAMP [42] software. RS were calculated using the diffraction elastic constants (DEC) for Inconel 718 $s_1^{hkl} = -1.523 \times 10^{-6}\,\text{MPa}^{-1}$ and $\frac{1}{2}s_2^{hkl} = 6.445 \times 10^{-6}\,\text{MPa}^{-1}$ according to Kröner [37] based on single crystals coefficients by Dye et al. [38]. The strain free lattice parameter d_0^{hkl} was analysed using cut-free cubes. The cubes were $2\,\text{mm} \times 2\,\text{mm} \times 2\,\text{mm}$ and EDM wire cut from twin samples for the substrate as well as for both process zones.

3. Results and discussion

3.1. Coating quality and bonding

BSE-SEM images of the microstructure are shown in Fig. 5. The micrographs are taken at a reasonable distance from the interface (see A-A reference in Fig. 3) for the substrate material as well as in the filled process zone for Parameter I and Parameter II. The results reveal a plastically deformed microstructure in the filling that is common for AE10718 particles deposited on Inconel 718 substrate material by CGS, as is discussed in literature e.g. [28,30,33]. Orientation contrast in the BSE mode enables the identification of individual grains in the substrate (Fig. 5a). Due to the high degree of plastic deformation the particles are subjected to during CGS, individual crystallites cannot be discerned by orientation contrast within the filled process zone (Fig. 5b, c). The Al-rich Ni solid solution particles can be distinguished from the surrounding material due to their darker appearance, which is a consequence of the materials contrast (Z-contrast) in BSE-SEM images. Metallographic analyses revealed no significant differences between the two parameters and a macroscopically homogeneous microstructure throughout the filled repair cavity.

In order to evaluate the bonding of the filler material to the surface of the cavity, SEM investigations were carried out along the interface for both parameters. Fig. 6 compares the results for both parameters at different locations along the interface. For both parameters the results show good bonding of the repair filling to the surrounding substrate material, even at locations where the spraying angle deviates from the optimum angle, i.e Fig. 6 blue and violet. These findings are in good agreement with results from previous studies on the repair of large cavities in flat specimens [25]. The narrow zone of approximately 40 µm on the substrate surface in which a microstructural change is visible is not the result of the cold gas spraying process, but comes from the shearing during the machining of the surface, i.e. from the milling out of the cavity. At the transition from the cylindrical surface to the repair site, the investigations, shown in Fig. 7 revealed delamination of the deposit for both parameters and on both sides of the cavity cross section. This behaviour might be due to the interaction of the gas stream with this specific geometric feature at the transition from cylindrical surface to the repair cavity. In addition to the spray angle not being the optimum of $\alpha_{spray} = 90°$ [33] at this location, the gas jet is likely to be deflected, which further impedes an efficient deposition of AE10718 particles onto the Inconel 718 substrate. A further potential cause may be that the adhesion strength at this location may not be sufficient to withstand the high stress gradients created by the CGS process and,

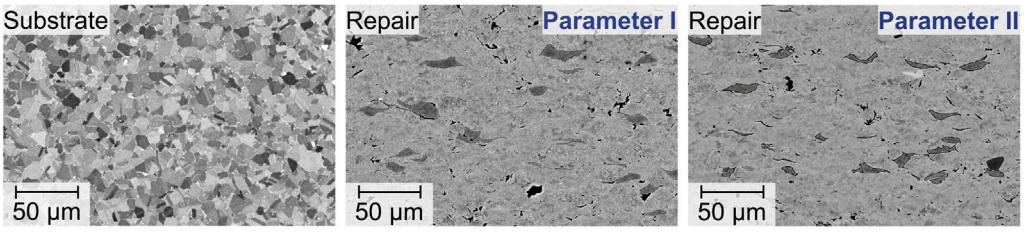

Fig. 5. BSE-SEM micrographs showing the substrate material (a), the repair filling for Parameter I (b) and the repair filling of Parameter II (c). All images are taken at a reasonable distance from the interface.

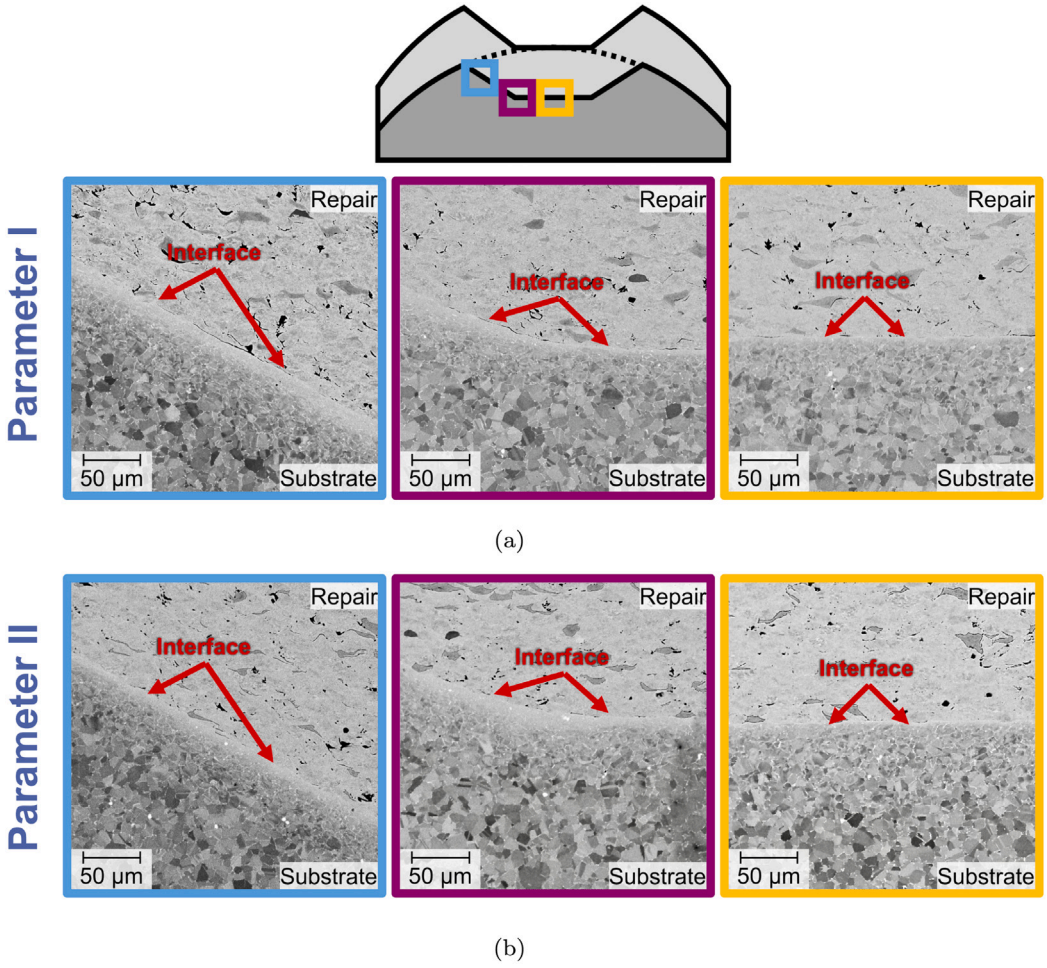

Fig. 6. Schematic representation of the cylindrical specimen's cross section (top) and BSE-SEM micrographs along the interface between repair filling and substrate along at the tapered sidewall (blue), the sidewall to ground transition (violet) and the cavity ground (yellow) for Parameter I (a) and Parameter II (b). The interface is highlighted in red.

consequently, leads to the local delamination of the deposit. This is emphasised by the findings in our previous work where a good bonding without delamination at the transition from substrate surface to repair cavity in case of a flat specimen geometry was observed, as presented in [25].

3.2. Microhardness mapping

Fig. 8 shows the Vickers microhardness (HV 0.1) map on the mid-plane cross section of the specimens (see A-A reference in Fig. 3) for Parameter I (a) and Parameter II (b). The shape of the cavity is indicated by a dashed line. The shaded markings indicate the specimen geometry beyond the measurement. The low-hardness white region in the top-centre location of the repair filling corresponds to the location of the bore hole from the incremental hole drilling analysis. After the residual stress analysis, the specimens were EDM wire cut and the sections were metallographically prepared, according to Section 2.2, before the microhardness analyses were performed. The results show a rather homogeneous Vickers microhardness distribution in the substrate as well as in the repair filling with a steep gradient between the two for both parameters, despite the high spatial resolution and the small indentation size. This is in agreement with the findings from the metallographic analyses in Section 3.1 and with the results for flat specimens presented in [25]. It can be surmised that variations in the mechanical boundary conditions of the substrate geometry have a negligible impact on the hardness and cold hardening properties of the repair filling. The average microhardness value in the substrate is $\approx 265 \pm 14$ HV 0.1, in the repair filling for Parameter I $\approx 511 \pm 43$ HV 0.1

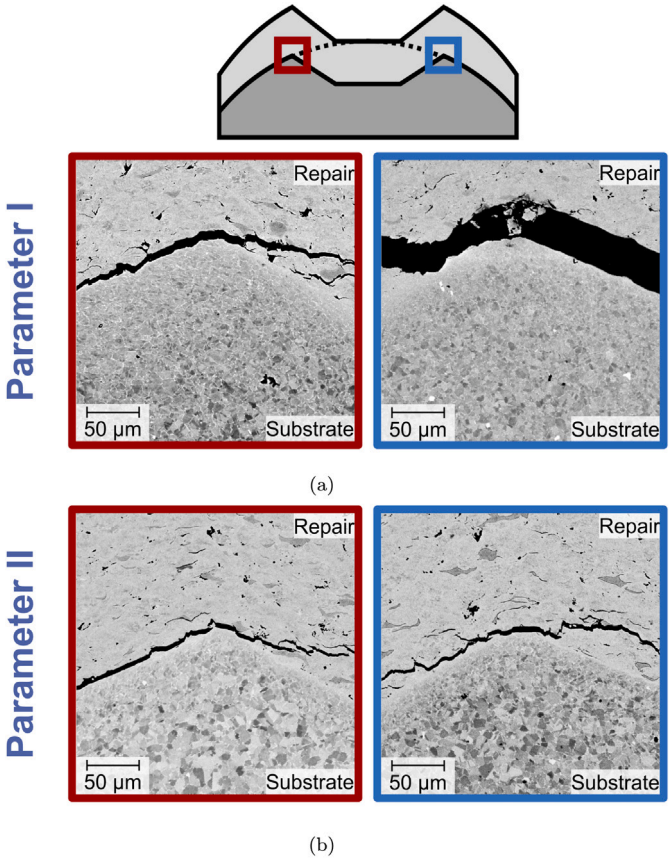

Fig. 7. Schematic representation of the cylindrical specimen cross section (top) and BSE-SEM micrographs at the transition from cylindrical surface to repair cavity for Parameter I (a) and Parameter II (b) on both sides of the cavity cross section.

and ≈537 ± 38 HV 0.1 in the repair filling of Parameter II. The hardness values in the process zone are in the range of precipitation hardened Inconel 718.

3.3. Incremental hole drilling analysis

The results of the near surface RS analysis from the incremental hole drilling analyses are presented in Fig. 9. The diagram shows the RS depth distribution for Parameter I (filled symbols) and Parameter II (unfilled symbols) in the x- (blue) and y-direction (green) of the samples in the as-sprayed condition in the centre of the repair cavity. The results show compressive RS in the repair filling for Parameter I with a rather homogeneous depth distribution in x- and in y-direction. The average compressive RS $\sigma_x^{avg} \approx -73 \pm 19$ MPa in x-direction are lower than $\sigma_y^{avg} \approx -256 \pm 44$ MPa in y-direction, which is in contrast to the direction independent RS distributions observed for AE10718 coatings deposited on planar Inconel 718 substrates by means of CGS in literature, e.g. [27,29]. This is due to the larger geometric constraints in y-direction, i.e. the length of the cavity L_c in relation to the width W_c. Such geometric constraints could also result in different temperature gradients in the two directions. For the second parameter however, the average RS $\sigma_x^{avg} \approx 22 \pm 29$ MPa in x-direction are tensile, which is attributed to the higher thermal input with Parameter II. This effect is consistent with the findings in [28]. In contrast, the average RS in y-direction $\sigma_y^{avg} \approx -262 \pm 40$ MPa are of compressive type and in the same range as for Parameter I. This emphasises the geometric influence on the RS distribution created by the elongated repair site.

3.4. Neutron diffraction residual stress analysis

Work hardening

The contour plots in Fig. 10 show the full width at half maximum (FWHM) of neutron diffraction lines, normalised to the FWHM of the powder prior to CGS for the specimens processed with Parameter I (a) and Parameter II (b), according to $normalised\,FWHM = \frac{FWHM}{FWHM_{powder}}$. The results for Parameter II are mirrored along the z-direction of the sample, for visualisation purposes. The hatched area marks the specimen, black crosses show the measurement locations and the shape of the repair cavity is marked by a dashed line. The graph reveals strongly broadened peaks within the filled process zone, a result of the high amount of plastic deformation the particles are subjected to during CGS. The average levels for the FWHM increase are comparable for Parameter I and Parameter II with an average FWHM increase of ≈1.72 ± 0.23 and ≈1.83 ± 0.18 for Parameter I and Parameter II, respectively. In both cases the distribution is almost homogeneous, which suggests a rather homogeneous state throughout the process zone. This is in agreement with the results from the metallographic analyses shown in Section 2.2.

Residual stress analysis

This work focuses on the RS distributions in the as-sprayed state of these two sample states and the comparison to the results for flat specimen geometries, with different mechanical constraints shown in our previous work [25]. The results of the triaxial RS distributions, analysed by neutron diffraction, are shown in Fig. 11 top, mid and bottom for the x, y and z-direction, respectively. The contour graphs show the RS maps for Parameter I (a) and Parameter II (b). The specimen beyond the mapping grid is represented by the hatched area. The measurement locations are marked by black crosses. The results reveal compressive RS throughout the process zone and balancing tensile RS in the substrate near the interface (c.f. A-A reference in Fig. 3), illustrated by a dashed line, of the as-sprayed condition for both parameters. In agreement with our results for the repair of cavities in flat specimens by means of CGS presented in [25], the highest compressive RS are in the y-direction of the sample with similar magnitudes $\sigma_{avg,y}^{ParameterI} \approx -308 \pm 72$ MPa and $\sigma_{avg,y}^{ParameterII} \approx -306 \pm 79$ MPa for Parameter I and Parameter II, respectively. In support of the findings of the RS analysis by incremental hole drilling analyses (c.f. Section 2.4) the RS are lower in the x-direction of the specimen. This could be caused by the different geometric constraints as a result of the elongated cavity shape, i.e. the relation of the length of the cavity L_C and the width W_C (c.f. Fig. 3). The compressive RS level in x-direction is lower for Parameter II ($\sigma_{avg,x}^{ParameterI} \approx -160 \pm 71$ MPa and $\sigma_{avg,x}^{ParameterII} \approx -141 \pm 91$ MPa for Parameter I and Parameter II, respectively) which can be attributed to the higher heat input in the sample processed with Parameter II as the gas temperature is higher (c.f Table 1). With regard to a further repair step, i.e. the machining to the final component shape, or thermal post-treatment, this could prove beneficial, due to a reduced risk of distortion. The results in the z-direction for both parameters (Fig. 11 bottom) demonstrate RS levels approaching zero in comparison to the other two directions, as well as a less uniform distribution. This may be attributed to the relatively low magnitude of strains in this direction and the increased diffraction line widths, which complicate the determination of exact peak positions. The level of balancing tensile RS near the interface is comparable for Parameter I and Parameter II with $\sigma_{avg,x}^{ParameterI} \approx 108 \pm 65$ MPa and $\sigma_{avg,x}^{ParameterII} \approx 108 \pm 59$ MPa in x-direction, $\sigma_{avg,y}^{ParameterI} \approx 89 \pm 70$ MPa and $\sigma_{avg,y}^{ParameterII} \approx 102 \pm 62$ MPa in y-direction, and $\sigma_{avg,z}^{ParameterI} \approx 51 \pm 77$ MPa and $\sigma_{avg,z}^{ParameterII} \approx 92 \pm 30$ MPa in z-direction. In the case of steep gradients (e.g. around the interface), the mapping grid smears out the results so that the exact extreme values cannot be mapped under certain circumstances.

Additional uncertainties in RS analyses by neutron diffraction experiments may be associated with relatively small gauge volume and

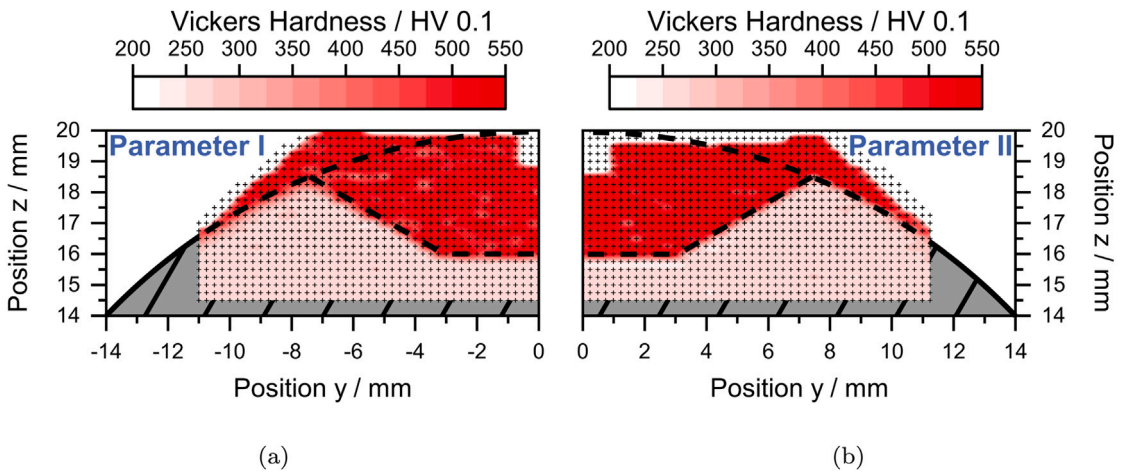

(a) (b)

Fig. 8. Vickers microhardness (HV 0.1) distribution on the mid-plane cross section of the repair cavity for Parameter I (a) and Parameter II (b). The surrounding substrate material beyond the measurement is represented by the hatched area. The geometry of the repair cavity and the cylindrical surface are marked with a dashed line. The individual measurement locations are represented by dots.

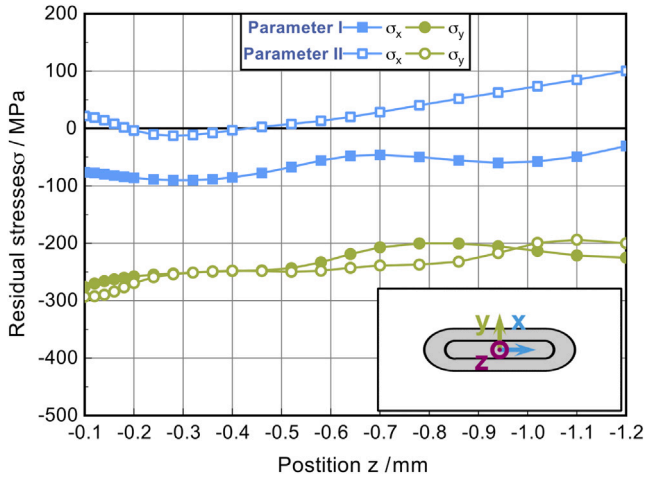

Fig. 9. Residual stress depth distribution analysed by means of incremental hole drilling analysis for Parameter I (filled symbols) and Parameter II (unfilled symbols) in x-direction (blue) and y-direction (green) of the sample (cf. Fig. 3).

the complexity in determining strain-free lattice spacing d_0^{hkl} in combination with an unfavourable geometry for diffraction experiments. The combination of measurement direction and measurement position can result in a notable increase in beam paths (secant line on the circular cross-section (c.f. A-A reference in Fig. 3)) within the specimen. This phenomenon results in enhanced absorption, which in turn attenuates the signal that can be detected. This renders the precise determination of peak positions challenging, thereby impeding the analysis of RS distributions. Consequently, the results of measurements may, on occasion, exhibit a notable degree of variability, as evidenced by the standard deviation of the data set. The maximum error in stress analysis is comparable in all three directions and accumulates to $\sigma^{error}_{substrate} \approx 34\,\text{MPa}$ and $\sigma^{error}_{filling} \approx 138\,\text{MPa}$ in the substrate and filling, respectively. Regardless of the higher uncertainties, the results from neutron diffraction RS analysis are in good agreement with results from incremental hole drilling analyses (see Section 3.3). Although these results are analysed closer to the specimen surface, the overall range of direction dependent compressive RS within the filled process zone is similar for both parameters. This provides a basis for confidence in the results of neutron diffraction.

In spite of the differences in the mechanical constraints imposed by the cylindrical specimens when compared to the flat specimens in a previous study [25], the neutron diffraction RS distribution results are in good agreement, which suggests that the delamination seen at the transition from cylindrical surface to the repair cavity (see Section 3.1) does not influence the final RS distribution throughout the 4 mm deep repair cavity.

4. Conclusion

A series of complementary RS analyses and metallographic studies were conducted on cylindrical Inconel 718 specimens, which feature elongated 4 mm deep tapered cavities filled with AE10781 powder via CGS. The principal conclusions that can be drawn are as follows:

- Cavities with a depth of $D_C = 4\,\text{mm}$ on the surface of cylindrical specimens made from Inconel 718 can be repaired with powder, having a chemical composition similar to Inconel 718, using CGS in combination with two different spraying parameters.
- Both Parameter I and Parameter II exhibit a rather homogeneous microstructure with strong plastic deformation throughout the filled process zone. This homogeneous state is further emphasised by the uniform microhardness distribution as well an almost homogeneous increase in the neutron diffraction line width (FWHM), resulting from the particle deformation during CGS deposition.
- Investigations along the interface suggest the bonding of filling to the surface of a large tapered cavity is good. Particularly at the tapered sidewalls of the cavity, where the deposition angle deviates from the optimum, and the transition from sidewall to cavity ground, that could promote vortexes, neither cracks nor delamination could be observed.
- At the transition from the cavity sidewall to the cylindrical sample surface, delamination occurred for both parameters. Further research is essential to gain a deeper understanding of the interaction between the cavity geometry and not only the CGS gas flow, but also the component to be repaired.
- The characterisation of the filled process zones and the surrounding substrates using neutron diffraction RS analysis revealed direction dependent compressive RS throughout the filling, as well as compensating tensile RS in the substrate in the vicinity of the interface in the as-sprayed condition. These findings are corroborated by complementary incremental hole drilling analysis near the surface of the filled cavity, which revealed direction dependent, almost constant RS depth profiles for both parameters.

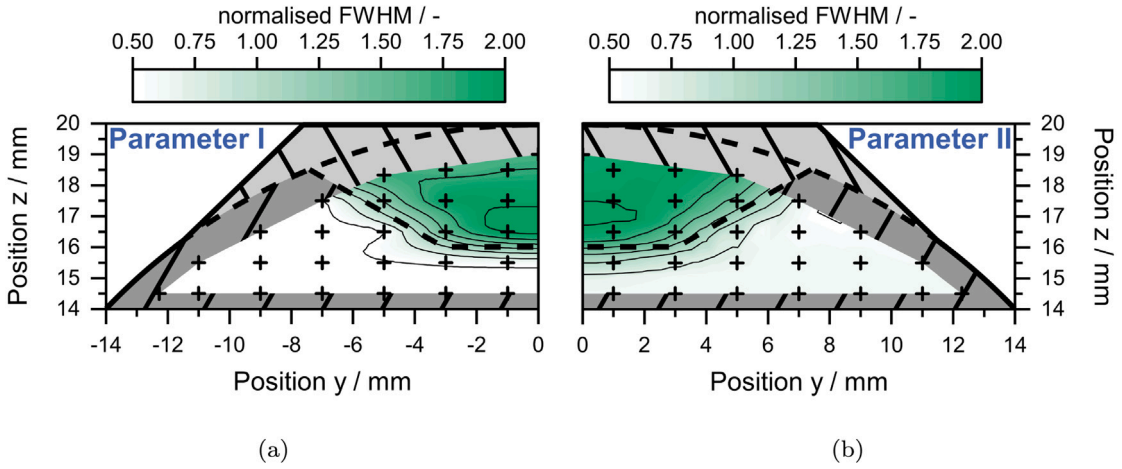

Fig. 10. Contour graph of the normalised FWHM for Parameter I (a) and Parameter II (b), determined by neutron diffraction. The FWHM is normalised to the FWHM of the powder before CGS. The dark, hatched area illustrates the substrate material, while the light, hatched area represents the CGS deposit in the as-sprayed state. The dashed line marks the cylindrical outline of the sample as well as the repair cavity. The measurement locations are depicted by black crosses. For visualisation purposes, the data for Parameter II are mirrored with respect to the symmetry axis.

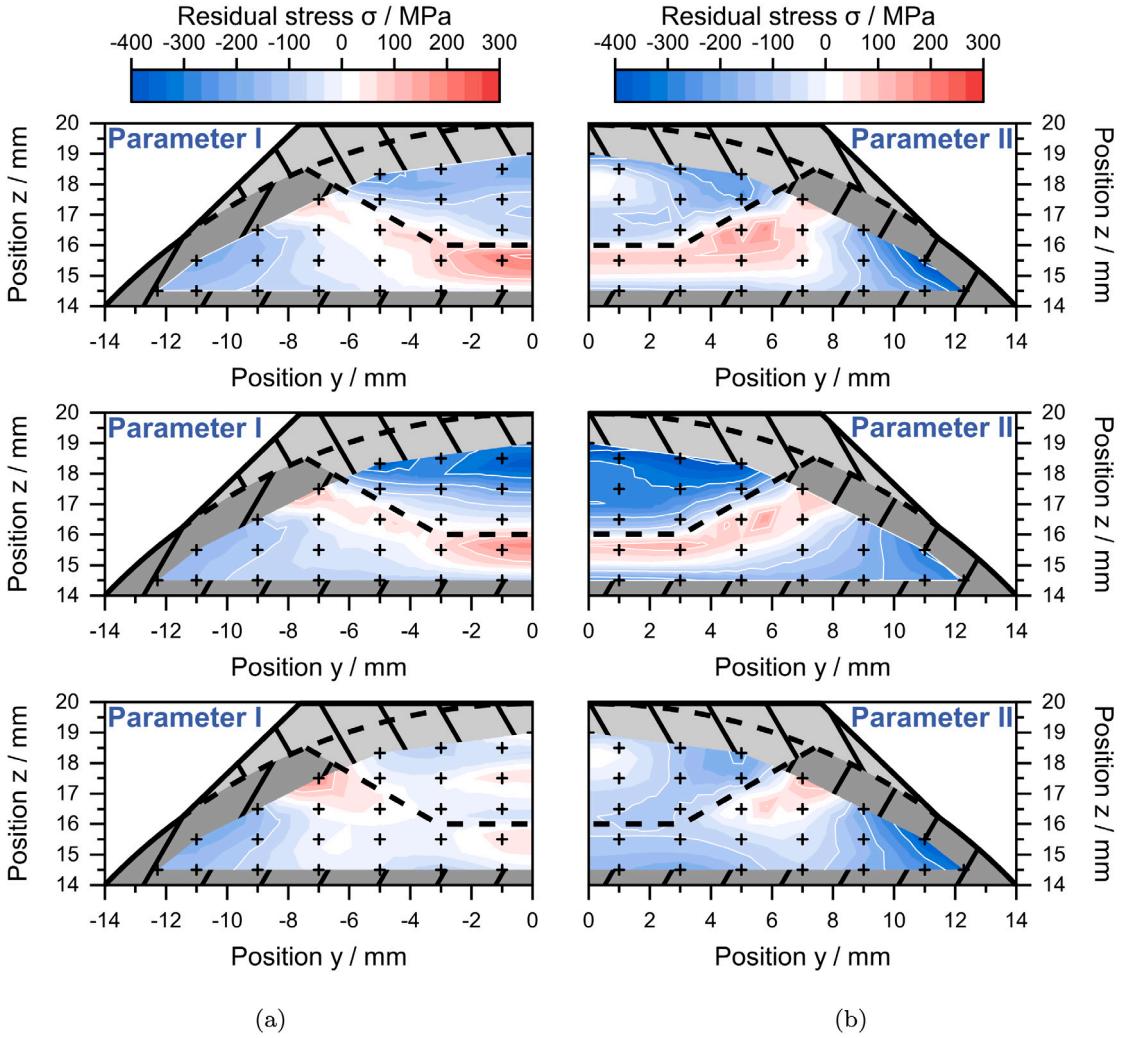

Fig. 11. Contour graphs showing the triaxial residual stress distribution for Parameter I (a) and Parameter II (b), in *x*-direction (top), *y*-direction (mid) and *z*-direction (bottom). The dark, hatched area illustrates the substrate material, while the light, hatched area represents the CGS deposit in the as-sprayed state. The dashed line marks the cylindrical outline of the sample as well as the repair cavity. The measurement locations are depicted by black crosses. For visualisation purposes, the data for Parameter II are mirrored with respect to the symmetry axis.

- Overall, these observations are in good agreement with the results obtained for the repair of deep cavities on flat samples made from Inconel 718, despite the delamination that occurred at the transition from cylindrical surface to repair cavity for both Parameter I and Parameter II. Although this might suggest, that the mechanical integrity is not jeopardised by this delamination, especially during the next repair step, i.e. the machining to the final shape geometry, this defect could have major impact.

CRediT authorship contribution statement

Florian Lang: Writing – review & editing, Writing – original draft, Visualization, Methodology, Investigation, Formal analysis, Data curation, Conceptualization. **Johannes-Christian Schmitt:** Writing – review & editing, Resources. **Thilo Pirling:** Resources, Investigation. **Robert Vaßen:** Resources, Project administration, Funding acquisition. **Jens Gibmeier:** Writing – review & editing, Supervision, Resources, Project administration, Funding acquisition.

Declaration of Generative AI and AI-assisted technologies in the writing process

During the preparation of this work the authors used DeepL in order to improve the readability and language of the manuscript. After using this tool/service, the authors reviewed and edited the content as needed and take full responsibility for the content of the published article.

Funding

This project was funded by the German Research Foundation (DFG) through the project 452606919.

Declaration of competing interest

The authors declare that they have no known competing financial interests or personal relationships that could have appeared to influence the work reported in this paper.

Acknowledgements

The authors are grateful to the Institut Laue-Langevin for granting beam time [41] at the SALSA instrument and their technical support.

Data availability

Data will be made available on request.

References

[1] J. Villafuerte (Ed.), Modern Cold Spray, Springer International Publishing, Cham, 2015, http://dx.doi.org/10.1007/978-3-319-16772-5.

[2] J.W. Murray, M.V. Zuccoli, T. Hussain, Heat treatment of cold-sprayed C355 Al for repair: Microstructure and mechanical properties, J. Therm. Spray Technol. 27 (2018) 159–168, http://dx.doi.org/10.1007/s11666-017-0665-z.

[3] R. Ghelichi, D. MacDonald, S. Bagherifard, H. Jahed, M. Guagliano, B. Jodoin, Microstructure and fatigue behavior of cold spray coated Al5052, Acta Mater. 60 (2012) 6555–6561, http://dx.doi.org/10.1016/j.actamat.2012.08.020.

[4] P. Cavaliere (Ed.), Cold-Spray Coatings: Recent Trends and Future Perspectives, Springer International Publishing, Cham, 2017, http://dx.doi.org/10.1007/978-3-319-67183-3.

[5] H. Assadi, F. Gärtner, T. Stoltenhoff, H. Kreye, Bonding mechanism in cold gas spraying, Acta Mater. 51 (2003) 4379–4394, http://dx.doi.org/10.1016/S1359-6454(03)00274-X.

[6] T. Schmidt, H. Assadi, F. Gärtner, H. Richter, T. Stoltenhoff, H. Kreye, T. Klassen, From particle acceleration to impact and bonding in cold spraying, J. Therm. Spray Technol. 18 (2009) 794–808, http://dx.doi.org/10.1007/s11666-009-9357-7.

[7] V.K. Champagne, The Cold Spray Materials Deposition Process, Woodhead Publishing Limited, Cambridge, England, 2007, http://dx.doi.org/10.1533/9781845693787.

[8] M. Grujicic, C.L. Zhao, W.S. DeRosset, D. Helfritch, Adiabatic shear instability based mechanism for particles/substrate bonding in the cold-gas dynamic-spray process, Mater. Des. 25 (2004) 681–688, http://dx.doi.org/10.1016/J.MATDES.2004.03.008.

[9] C.A. Widener, M.J. Carter, O.C. Ozdemir, R.H. Hrabe, B. Hoiland, T.E. Stamey, V.K. Champagne, T.J. Eden, Application of high-pressure cold spray for an internal bore repair of a navy valve actuator, J. Therm. Spray Technol. 25 (2016) 193–201, http://dx.doi.org/10.1007/s11666-015-0366-4.

[10] R.F. Vaz, A. Garfias, V. Albaladejo, J. Sanchez, I.G. Cano, A review of advances in cold spray additive manufacturing, Coatings 13 (2023) 267, http://dx.doi.org/10.3390/COATINGS13020267, 2023, Vol. 13, Page 267.

[11] K. Petráčková, J. Kondás, M. Guagliano, Fixing a hole (with cold spray), Int. J. Fatigue 110 (2018) 144–152, http://dx.doi.org/10.1016/j.ijfatigue.2018.01.014.

[12] O. Stier, Fundamental cost analysis of cold spray, J. Therm. Spray Technol. 23 (2014) 131–139, http://dx.doi.org/10.1007/s11666-013-9972-1.

[13] M. Faccoli, G. Cornacchia, D. Maestrini, G.P. Marconi, R. Roberti, Cold spray repair of martensitic stainless steel components, J. Therm. Spray Technol. 23 (2014) 1270–1280, http://dx.doi.org/10.1007/s11666-014-0129-7.

[14] E. Rúa Ramirez, A. Silvello, E. Torres Diaz, R.F. Vaz, I.G. Cano, A comparative study of the life cycle inventory of thermally sprayed WC-12Co coatings, Metals 14 (2024) 431, http://dx.doi.org/10.3390/MET14040431, 2024, Vol. 14, Page 431.

[15] S. Dosta, M. Couto, J.M. Guilemany, Cold spray deposition of a WC-25Co cermet onto Al7075-T6 and carbon steel substrates, Acta Mater. 61 (2013) 643–652, http://dx.doi.org/10.1016/J.ACTAMAT.2012.10.011.

[16] N. Cinca, J. Guilemany, Cold gas sprayed stellite-6 coatings and their wear resistance, J. Mater. Sci. Eng. 02 (2013) http://dx.doi.org/10.4172/2169-0022.1000122.

[17] V.K. Champagne, D.J. Helfritch, A demonstration of the antimicrobial effectiveness of various copper surfaces, J. Biol. Eng. 7 (2013) http://dx.doi.org/10.1186/1754-1611-7-8.

[18] A. Farjam, Y. Cormier, P. Dupuis, B. Jodoin, A. Corbeil, Influence of alumina addition to aluminum fins for compact heat exchangers produced by cold spray additive manufacturing, J. Therm. Spray Technol. 24 (2015) 1256–1268, http://dx.doi.org/10.1007/s11666-015-0305-4.

[19] V. Luzin, O. Kirstein, S.H. Zahiri, D. Fraser, Residual stress buildup in Ti components produced by cold spray additive manufacturing (CSAM), J. Therm. Spray Technol. 29 (2020) 1498–1507, http://dx.doi.org/10.1007/s11666-020-01048-z.

[20] A. Vargas-Uscategui, P.C. King, M.J. Styles, M. Saleh, V. Luzin, K. Thorogood, Residual stresses in cold spray additively manufactured hollow titanium cylinders, J. Therm. Spray Technol. 29 (2020) 1508–1524, http://dx.doi.org/10.1007/s11666-020-01028-3.

[21] S. Yin, P. Cavaliere, B. Aldwell, R. Jenkins, H. Liao, W. Li, R. Lupoi, Cold spray additive manufacturing and repair: Fundamentals and applications, Addit. Manuf. 21 (2018) 628–650, http://dx.doi.org/10.1016/j.addma.2018.04.017.

[22] V.K. Champagne, O.C. Ozdemir, A. Nardi (Eds.), Practical Cold Spray, Springer International Publishing, Cham, 2021, http://dx.doi.org/10.1007/978-3-030-70056-0.

[23] B.L. James, B-1 cold spray initiative, in: Cold Spray Action Team Meeting 2016, Cold Spray Action Team Meeting, Worcester, MA, USA, 2016, URL: https://www.coldsprayteam.com/2016csatmeeting.html.

[24] C.A. Widener, R.H. Hrabe, B. James, V.K. Champagne, B1 bomber-FEB panel repair by cold spray, in: Cold Spray Action Team (CSAT) Meeting 2013 (Worcester Polytechnic Institute, MA, 2013), Worcester, MA, USA, 2013.

[25] F. Lang, J.-C. Schmitt, S. Cabeza, T. Pirling, J. Fiebig, R. Vassen, J. Gibmeier, IN718 cold gas repair spray of large cavities—Microstructure and residual stresses, in: The Minerals, Metals & Materials Series, Springer, Cham, 2023, pp. 739–753, http://dx.doi.org/10.1007/978-3-031-27447-3{_}44.

[26] D. Boruah, B. Ahmad, T.L. Lee, S. Kabra, A.K. Syed, P. McNutt, M. Doré, X. Zhang, Evaluation of residual stresses induced by cold spraying of Ti-6Al-4V on Ti-6Al-4V substrates, Surf. Coat. Technol. 374 (2019) 591–602, http://dx.doi.org/10.1016/j.surfcoat.2019.06.028.

[27] R. Vassen, J. Fiebig, T. Kalfhaus, J. Gibmeier, A. Kostka, S. Schrüfer, Correlation of microstructure and properties of cold gas sprayed INCONEL 718 coatings, J. Therm. Spray Technol. 29 (2020) 1455–1465, http://dx.doi.org/10.1007/s11666-020-00988-w.

[28] J. Schmitt, J. Fiebig, S. Schrüfer, O. Guillon, R. Vaßen, Adjusting residual stresses during cold spray deposition of IN718, J. Therm. Spray Technol. 33 (2024) 210–220, http://dx.doi.org/10.1007/s11666-023-01673-4.

[29] R. Singh, S. Schruefer, S. Wilson, J. Gibmeier, R. Vassen, Influence of coating thickness on residual stress and adhesion-strength of cold-sprayed inconel 718 coatings, Surf. Coat. Technol. 350 (2018) 64–73, http://dx.doi.org/10.1016/j.surfcoat.2018.06.080.

[30] J. Fiebig, E. Bakan, T. Kalfhaus, G. Mauer, O. Guillon, R. Vassen, Thermal spray processes for the repair of gas turbine components, Adv. Eng. Mater. 22 (2020) 1901237, http://dx.doi.org/10.1002/ADEM.201901237.

[31] R. Vassen, J.-C. Schmitt, J. Fiebig, M. Létang, F. Lang, J. Gibmeier, S. Schrüfer, Reparatur von nickelbasislegierungen mit hoch-kinetischen thermischen spritzverfahren, in: C. Penszoir, W. Krömmer (Eds.), 12. Kolloquium Hochgeschwindigkeits-Flammspritzen 2023, Gemeinschaft Thermisches Spritzen e.V. Erding, 2023, pp. 43–52.

[32] S. Wilson, A. Barth, M. Nestler, S. Kupada, Cold gas spray coating methods and compositions, 2015, patent application, WO 2017/003427 A1.

[33] R. Singh, K.-H.H. Rauwald, E. Wessel, G. Mauer, S. Schruefer, A. Barth, S. Wilson, R. Vassen, Effects of substrate roughness and spray-angle on deposition behavior of cold-sprayed Inconel 718, Surf. Coat. Technol. 319 (2017) 249–259, http://dx.doi.org/10.1016/j.surfcoat.2017.03.072.

[34] DIN EN ISO 6507-1:2018-07, metallische werkstoffe - härteprüfung nach vickers - teil 1: Prüfverfahren, 2018, http://dx.doi.org/10.31030/2778746.

[35] ASTM 837-20, Standard test method for determining residual stresses by the hole-drilling strain-gages, 2020, http://dx.doi.org/10.1520/E0837-20.

[36] T. Schwarz, H. Kockelmann, Die bohrlochmethode–ein für viele anwendungsbereiche optimales verfahren zur experimentellen ermittlung von eigenspannungen, Messtech. Briefe 29 (1993) 33–38.

[37] E. Kröner, Berechnung der elastischen konstanten des vielkristalls aus den konstanten des einkristalls, Z. Phys. 151 (1958) 504–518, http://dx.doi.org/10.1007/BF01337948.

[38] D. Dye, S.M. Roberts, P.J. Withers, R.C. Reed, The determination of the residual strains and stresses in a tungsten inert gas welded sheet of IN718 superalloy using neutron diffraction, J. Strain Anal. Eng. Des. 35 (2000) 247–259, http://dx.doi.org/10.1243/0309324001514396.

[39] T. Pirling, G. Bruno, P.J. Withers, SALSA: Advances in residual stress measurement at ILL, Mater. Sci. Forum 524–525 (2006) 217–222, http://dx.doi.org/10.4028/www.scientific.net/MSF.524-525.217.

[40] M.T. Hutchings, Neutron diffraction measurement of residual stress fields—The answer to the engineers' prayer? Nondestruct. Test. Eval. 5 (1990) 395–413, http://dx.doi.org/10.1080/02780899008952981.

[41] J. Gibmeier, S. Cabeza, F. Lang, Triaxial residual stress distributions after local repair of practice-relevant components by means of cold gas repair spraying, 2023, http://dx.doi.org/10.5291/ILL-DATA.1-02-358.

[42] D. Richard, M. Ferrand, G.J. Kearley, Analysis and visualisation of neutron-scattering data, J. Neutron Res. 4 (1996) 33–39, http://dx.doi.org/10.1080/10238169608200065.